JOURNAL OF PROPULSION AND POWER
Vol. 22, No. 3, May–June 2006

Magnetohydrodynamic Energy-Bypass Procedure in a Three-Dimensional Scramjet

Datta V. Gaitonde*
Air Force Research Laboratory, Wright–Patterson AFB, Ohio 45433

A generic configuration is employed to explore the kinematic and dynamic structure of the flowfield in a Mach 8 scramjet with and without magnetohydrodynamic (MHD-) bypass. Particular emphasis is placed on describing the three-dimensional interaction between the fluid and the electromagnetic field in a given plasma environment. Faraday-type operation is considered with coarsely segmented electrodes in a generator and accelerator respectively mounted on either side of a constant-area isolator/combustor element. The numerical procedure adopts a robust high-resolution technique to solve the governing equations, which include the full three-dimensional Navier–Stokes equations supplemented with electromagnetic source terms and a Poisson equation for consistency of the electric field with current continuity. Spatially variable combustion and plasma parameters are either specified or phenomenologically derived. Various three-dimensional features such as swept shock-wave boundary layer interactions have a profound impact on operation. Separated regions and vortical structures interface with the current, electric, and ponderomotive force fields to yield complex three-dimensional features that indicate that two-dimensional and inviscid analyses are inappropriate. The MHD generator shows the potential to efficiently slow down flow in the inlet, thus decreasing scramjet inlet length, and to reduce the total temperature of the flow. However, separation causes near-wall secondary eddy currents and local body force reversal, thus limiting the useful length of the generator. Accelerator operation is characterized by more prominent irreversibilities, especially near walls, where electric and body force field gradients are large. Trends in integrated pressure and viscous and magnetic force are summarized.

Nomenclature

A	=	conductivity peak
a	=	width of conductivity distribution
$\boldsymbol{B}$	=	magnetic induction vector
$\mathrm{d}A$	=	differential area
e	=	energy
$\boldsymbol{E}$	=	electric field vector
F_B^*	=	magnetic force
F_p^*	=	pressure force
$\hat{F}, \hat{G}, \hat{H}$	=	flux vectors
I_s	=	ion-slip parameter
J	=	metric Jacobian
$\boldsymbol{j}$	=	current vector
K	=	load factor
M	=	Mach number
$\boldsymbol{n}$	=	normal vector
p	=	pressure
Pr	=	Prandtl number
Q	=	interaction parameter
Q_C	=	combustion heat source term
Q_{ht}	=	heat conduction term
R_b	=	magnetic pressure number
R_H	=	Hall parameter
R_σ	=	magnetic Reynolds number
Re	=	Reynolds number
$\hat{S}$	=	source term in flux equation
s	=	distance variable
t	=	time
$\boldsymbol{U}$	=	velocity vector
w	=	width of channel
$\hat{X}$	=	solution vector
α	=	ion-slip coefficient
β	=	Hall coefficient
δ	=	conductivity decay location
ϵ	=	conductivity decay value
ξ, η, ζ	=	transformed coordinates
ρ	=	density
$\tilde{\tilde{\sigma}}$	=	conductivity tensor
$\bar{\bar{\tau}}$	=	shear stress tensor
ϕ	=	electric potential

Subscript

I	=	inviscid
V	=	viscous
ref	=	reference

Received 17 November 2004; revision received 26 September 2005; accepted for publication 26 September 2005.

*Technical Area Leader, Computational Sciences Branch, Aeronautical Sciences Division, Air Vehicles Directorate. Associate Fellow AIAA.

I. Introduction

THE advantages of air-breathing propulsion, particularly with scramjet devices, are attractive in the quest for sustained hypersonic flight and routine, affordable access-to-space capability. However, significant challenges need to be overcome, including high heat loads and combustion inefficiencies, which require major advances in hypersonic flow control before a successful design can be proposed. Flow field modification techniques with magnetic fields have received increasing attention due to their potential for exerting body forces and energetic interactions without moving wetted parts. Several recent efforts[1–5] have emphasized different small- and large-scale flow-control possibilities, including inlet shock positioning for mass capture, heat load alleviation, control of fluid dynamic bifurcation, and energy management with the so-called magnetohydrodynamic (MHD) energy-bypass procedure.[3,6,7] These and other efforts have refined the parameter space of operation by considering ionization budgets, magnetic field magnitudes, and physical component details such as electrode design and placement.

Despite these advances, many uncertainties persist in the knowledge base and have precluded unambiguous determination of engineering feasibility. In particular, the detailed nature of three-dimensional fluid–electromagnetic interactions and their scaling

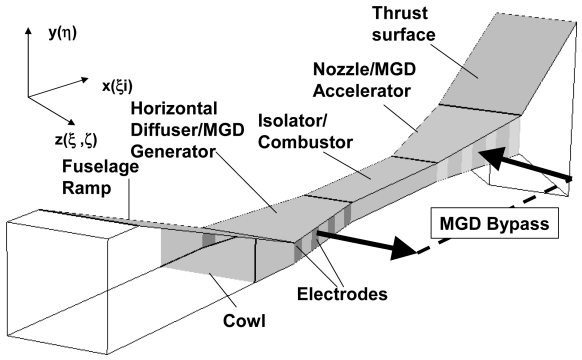

a) Dual-plane compression design (aspect ratio is 1:2:2)

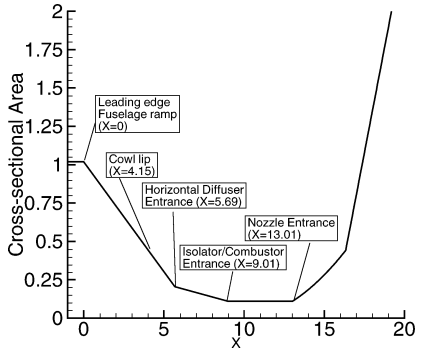

b) Nondimensional cross-sectional area variation

Fig. 1 Simulated flow-through scramjet configuration.

laws and optimal configuration details remain largely unknown. The difficulty can only be overcome by extensive experimentation and simultaneous development and application of new and self-consistent high-fidelity simulation tools that exploit modern computational techniques. This paper describes a preliminary numerical effort to explore the fluid dynamics of scramjet internal flows and their interaction with a specified plasma and combustion environment. Of the various possible uses of magnetic forces, we consider the MHD energy-bypass procedure, which has been described in Refs. 6, 7, for example. Although many variants of the configuration have been proposed, we consider that depicted in Fig. 1. The design comprises of a dual-plane compression inlet system followed by a constant-area isolator/combustor, nozzle, and thrust surface. The normalized cross-sectional area variation versus streamwise distance is depicted in Fig. 1b. The simplified design is well suited to explore the generic three-dimensional features likely to be encountered in a scramjet but isolated from the overwhelming geometrical complexity of an actual device. A recent effort at simulating bulk effects in MHD, with a view to determining flowfield acceleration, may be found in Ref. 8.

For the MHD-bypass procedure, a generator is mounted in the converging-sidewall inlet duct, with current being drawn through segmented electrodes. Theoretical considerations suggest that this procedure can reduce kinetic energy of the flow in the inlet through a more efficient procedure than if shock waves were employed for the same purpose, thus reducing distortion and losses, enhancing quality of flow for combustion, and reducing the size of the inlet. The extracted energy may be used either for onboard purposes, or to accelerate fluid in the accelerator to enhance thrust. Such a device is also considered in Fig. 1 in the expanding nozzle region downstream of the constant-area combustor. Further description is deferred to Section II.

In addition to the Mach (M), Reynolds (Re), and Prandtl (Pr) numbers encountered in traditional fluid dynamics, the principal parameters of interest include the magnetic Reynolds (R_σ) and pressure numbers (R_b) and their product, the interaction parameter (Q). The aerospace environment of interest is characterized by relatively low conductivity ($R_\sigma \ll 1$), which must be compensated for by a large magnetic field ($R_b \gg 1$) to obtain reasonable fluid–magnetic field interaction ($Q \sim O(1)$). A three-dimensional self-consistent fluid and plasma simulation remains unfeasible in the near future because of the daunting requirements for modeling and computational resources. Thus, in this effort, a model invoking a suitable combination of first principles and empirical elements is employed. Section III outlines the governing equations for the fluid and its interaction with the plasma environment. This includes the phenomenological implementation of the generalized Ohm's law and the current continuity equation for electric potential and field. The numerical method adopts a general curvilinear coordinate transformation together with techniques adapted from computational fluid dynamics (CFD),[9–11] with special emphasis on development of boundary conditions, as also described in Section III. Efforts to verify various components of the algorithm are also outlined in Section III.

Table 1 Cases computed

Case	AD[a]	Heat addition	Q[b]
A	Baseline ("Lam")	No	0
B	Ht add	Yes	0
C	MHD	Yes	1

[a] AD = alternative designation. [b] Q = interaction parameter.

To isolate physical effects with and without MHD, several computations of increasing complexity are performed, as summarized in Table 1. The first case, the baseline (denoted Case A or "Lam"), consists of flow through the device without control or heat addition. The effect of heat addition is then explored by considering a specified combustion profile (Case B or "Ht Add"). Case C ("MHD") considers MHD-bypass effects with the specified electrode configuration and potentials, an assumed ionization profile corresponding to e-beams in the general fashion described in Refs. 1, 3, and an interaction parameter of unity. Section V describes results by integrating the kinematics and dynamics (Section V.A), with electromagnetic field descriptions (Section V.B), energetic interactions (Section V.C), and integrated parameters (Section V.D).

II. Scramjet Configuration

The simulation is performed in terms of nondimensional parameters. The freestream Mach number is chosen to be $M = 8$, whereas the Reynolds number, based on the upstream width of the configuration, 0.6 m, is $Re = 1.6 \times 10^6$. Under typical low-enthalpy wind-tunnel conditions, high-temperature effects are anticipated to be relatively small. Factoring in the local environment in the generator, which is located downstream of the pitch plane shock system, an interaction parameter of unity as employed in Case C corresponds to a value of $\sigma B^2 \sim 100\ \text{mho} \cdot T^2$. Although these are relatively large values of the plasma parameters, they are in the same range as employed in system-level and conceptual studies forwarded in the literature.[1,2]

As noted earlier, the inlet of the chosen configuration, Fig. 1, employs dual-plane compression,[2] consisting of a vertical diffuser followed by a horizontal diffuser (HD). The pitch-plane shock from the ramp (8-deg angle) reflects off the cowl lip, at which station sidewalls are assumed to start. The fuselage ramp terminates at the point where the shock reflected from the cow llip intersects the upper wall. The sidewalls of the HD are inclined at 4 deg to the freestream. The resulting swept spanwise shock waves facilitate the evolution of a highly three-dimensional flow at the entrance of the constant-area isolator, which starts where the crossing shocks (from inviscid estimates) reach the opposite walls. The isolator and combustor are represented by a constant-area duct extending 4 streamwise-distance units. A nozzle with 4-deg diverging wall angles for all but the lower surface (which does not diverge, to provide a straight underside) serves to expand the flow. The nozzle side and bottom surfaces terminate where the width of the configuration equals that at the entrance; this facilitates the possibility of ganging such engines in a side-by-side fashion. The last component, the thrust surface, corresponds to an assumed underside of the vehicle of sufficient length to ensure that the flow is overexpanded at the exit of the computational domain. The angles chosen for the inlet system were designed to reduce the Mach number from its freestream value of 8 to 4 at

the isolator entrance (based on a simplified quasi-one-dimensional inviscid analysis). The objective of the MHD generator is then to reduce this further to a value dependent on the interaction parameter as detailed later. The design of Fig. 1 differs from that employed for preliminary computations in Ref. 12 primarily in the nozzle region, which was reconfigured to overcome numerical instability encountered when MHD acceleration was attempted.

III. Governing Equations and Numerical Procedure

The low-magnetic-Reynolds-number (or source term) form is obtained by coupling the Navier–Stokes equations with ponderomotive force and energy interaction terms:

$$\frac{\partial \rho^*}{\partial t^*} + \nabla^* \cdot (\rho^* \boldsymbol{U}^*) = 0 \tag{1}$$

$$\frac{\partial \rho^* \boldsymbol{U}^*}{\partial t^*} + \nabla^* \cdot [\rho^* \boldsymbol{U}^* \bar{\bar{\boldsymbol{U}}}^* + p^* \bar{\bar{I}}] - \frac{1}{Re} \nabla^* \cdot \bar{\bar{\tau}}^* = Q(\boldsymbol{j}^* \times \boldsymbol{B}^*)$$

$$\frac{\partial \rho^* e^*}{\partial t^*} + \nabla^* \cdot \left[(\rho^* e + p^*) \boldsymbol{U}^* - \frac{1}{Re} (\boldsymbol{U}^* \cdot \bar{\bar{\tau}}^*) \right.$$

$$\left. - \frac{1}{(\gamma - 1) Pr M^2 Re} Q^*_{\text{ht}} \right] = Q(\boldsymbol{E}^* \cdot \boldsymbol{j}^*) + Q^*_C \tag{2}$$

The superscript $*$ denotes a nondimensional quantity, t is the time, ρ is the density, $\boldsymbol{U} = \{u, v, w\}$ is the velocity vector, p is the pressure, $\boldsymbol{B}$ and $\boldsymbol{E}$ are the magnetic and electric fields, respectively, Q_{ht} is the heat conduction term, Q_C is the energy source term due to combustion, $\bar{\bar{\tau}}$ is the shear stress tensor, and $e = p/(\gamma - 1)\rho + \boldsymbol{U}^2/2$ is the total energy per unit mass. The transport properties are the molecular viscosity μ, obtained with Sutherland's law, and the electrical conductivity σ. In addition to the Reynolds number, $Re = \rho_{\text{ref}} U_{\text{ref}} L_{\text{ref}}/\mu_{\text{ref}}$, Mach number, M, and Prandtl number, $Pr = \mu_{\text{ref}} C_p/k_{\text{ref}}$, an interaction parameter $Q = \sigma_{\text{ref}} B^2_{\text{ref}} L_{\text{ref}}/(\rho_{\text{ref}} U_{\text{ref}})$ appears in the source term. In the subsequent discussion, the superscript $(*)$ will be dropped and all quantities will be assumed to be nondimensional unless explicitly otherwise stated.

The electrical quantities appearing in these equations are σ, $\boldsymbol{B}$, $\boldsymbol{j}$, and $\boldsymbol{E}$. The method of specifying σ is deferred to Section IV. Because the induced magnetic field is negligible in the low-R_σ approximation, $\boldsymbol{B}$ is the known (imposed) field. The current $\boldsymbol{j}$ is obtained with the phenomenological form of the generalized Ohm's law[13]:

$$\boldsymbol{j} = \tilde{\tilde{\sigma}} \cdot [\boldsymbol{E} + \boldsymbol{U} \times \boldsymbol{B}] \tag{3}$$

Expressions for the three-dimensional conductivity tensor $\tilde{\tilde{\sigma}}$ include the Hall (R_H) and ion-slip (I_s) parameters. Here $R_H = \sigma_{\text{ref}} \beta_{\text{ref}} B_{\text{ref}}$ and $I_s = \sigma_{\text{ref}} \alpha_{\text{ref}} B^2_{\text{ref}}$, where β and α are the Hall and ion-slip coefficients elsewhere.[14] The impact of these, particularly the Hall component of the current, can be significant[15] for the scramjet under consideration. Indeed, the main reason to utilize segmented instead of continuous electrodes is to minimize the impact of Hall currents, which are described in Refs. 16, 17.

The electric field $\boldsymbol{E}$ is determined from the current continuity condition:

$$\nabla \cdot \boldsymbol{j} = 0 \tag{4}$$

Introducing a scalar potential, $\boldsymbol{E} = -\nabla\phi$, the equation solved is

$$\nabla \cdot [\tilde{\tilde{\sigma}} \cdot [\nabla\phi]] = \nabla \cdot [\tilde{\tilde{\sigma}} \cdot \boldsymbol{U} \times \boldsymbol{B}] \tag{5}$$

Algebraic manipulation permits the fluid dynamic equations to be written in flux vector form as

$$\frac{\partial \hat{X}}{\partial t} + \frac{\partial \hat{F}_I}{\partial \xi} + \frac{\partial \hat{G}_I}{\partial \eta} + \frac{\partial \hat{H}_I}{\partial \zeta} = \frac{\partial \hat{F}_V}{\partial \xi} + \frac{\partial \hat{G}_V}{\partial \eta} + \frac{\partial \hat{H}_V}{\partial \zeta} + \hat{S} \tag{6}$$

where a general curvilinear coordinate transformation has been introduced, $x = x(\xi, \eta, \zeta)$, $y = y(\xi, \eta, \zeta)$, and $z = z(\xi, \eta, \zeta)$, to facilitate the treatment of complex configurations. The solution vector, X, is $1/J\{\rho, \rho u, \rho v, \rho w, \rho e\}$, where J is the Jacobian of the coordinate transformation. F_I, G_I, and H_I contain terms relevant to inviscid fluxes, F_V, G_V, and H_V include effects due to viscosity and thermal conductivity, and S is the source term containing electromagnetic interaction terms. The various vectors of Eq. 6 have been detailed in Refs. 9, 11.

Because the influence of the magnetic field is restricted to the source term in the present low-R_σ approach, conventional CFD techniques have been incorporated.[9,10] All results presented in this paper were obtained with the Roe scheme[18] to nominal third-order accuracy, together with a harmonic limiter to enforce monotonicity.[9]

To develop a solution procedure that exploits commonality with mature potential-flow solution procedures for the Poisson equation, Eq. (4) for the scalar ϕ may be written in a form similar to Eq. (6),

$$\frac{\partial}{\partial \tau}\left(\frac{\phi}{J}\right) + \frac{\partial \hat{F}}{\partial \xi} + \frac{\partial \hat{G}}{\partial \eta} + \frac{\partial \hat{H}}{\partial \zeta} = 0 \tag{7}$$

where the artifical time term is added in the manner of Ref. 19. In contrast to Eqs. (1) and (2), which used an upwind method, spatial discretization of the terms in Eq. (7) is accomplished with fourth-order compact differences as described in Ref. 11. Because the flow field contains shocks, high-order differencing of the right-hand side of Eq. (5) can introduce numerical instabilities. In such cases, smoothing is applied with a Pade-type filter, as described in more detail in Ref. 11. To develop the time-integration procedure, Eqs. (6) and (7) are linearized and approximately factored. The fluid and potential equations require the solution of block[20] and scalar[19] tridiagonal matrices respectively, as detailed in Ref. 14.

The code employed to solve these equations has been verified in various canonical subelements of the composite scramjet of Fig. 1. Results for a flat plate boundary layer subject to a magnetic field have been successfully compared with similarity theory in Ref. 9. Aspects of channel flows bounded by segmented electrodes have also been compared to theory and previous simulations by other researchers in Ref. 10. The ability of the method to accurately capture the sharp gradients of electric potential and the consistent buildup of electric field at electrode–insulator junctures was successfully demonstrated together with various effects that are also observed in the full scramjet, such as field reversal near electrodes. Another key phenomenon anticipated in the scramjet is the combination of events termed swept shock/boundary layer interactions. A series of previous papers (e.g., Refs. 21, 22) has demonstrated the capability of the scheme, through exhaustive comparison with experiment, to capture the key features of such flows, including three-dimensional separation, attachment, and vortex–shock interactions. As will be evident later, each of these structures is encountered in the chosen scramjet.

The grid on which most computations are reported (Fig. 2) consists of $299 \times 61 \times 61$ points and is constructed by stacking $x = constant$ Cartesian planes, within each of which nonuniform distributions are imposed in the y and z directions for clustering

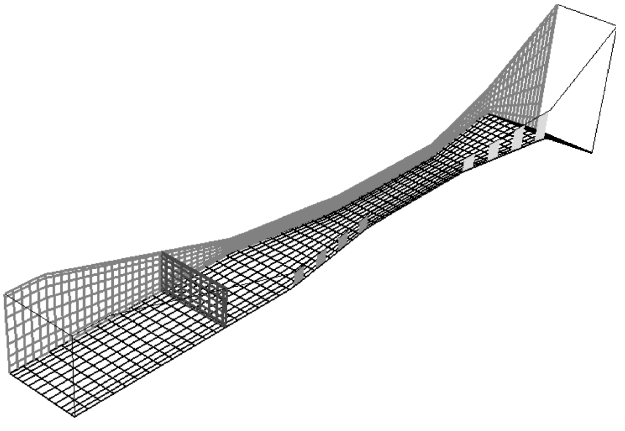

Fig. 2 Grid structure (coarsened for display).

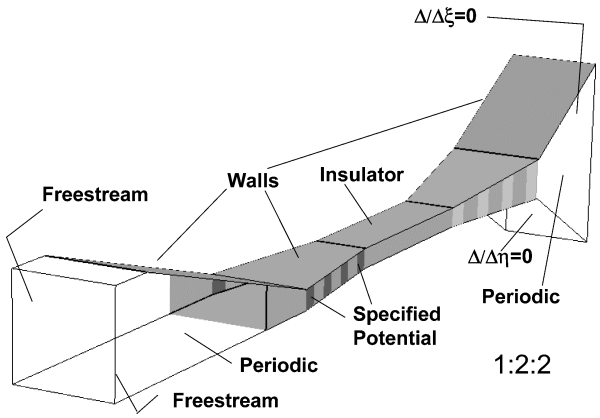

Fig. 3 Schematic of boundary conditions.

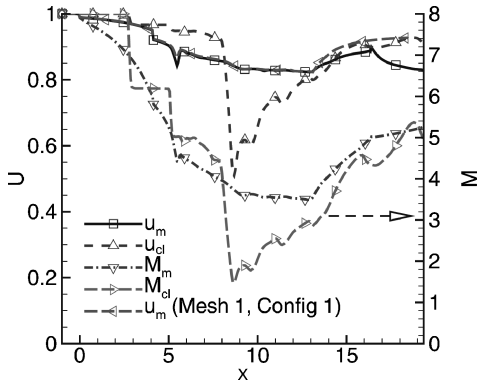

Fig. 4 Velocity and Mach number profiles for Case A (baseline flow).

near the surfaces. Electrode/insulator junctures are assumed to lie along grid lines to facilitate the imposition of potentials. To evaluate solution dependence on the grid, a simulation is also performed on a coarser mesh of $201 \times 41 \times 41$ points.

Boundary conditions are summarized in Fig. 3. The fluid dynamic variables, $\boldsymbol{U}$, p, and T, are treated in the same manner as in the no-MHD situation. On all solid surfaces, the no-slip condition is enforced, and the pressure gradient is set to zero. An adiabatic wall temperature condition is assumed. For all cases considered, the downstream boundaries are predominantly supersonic. Consequently, the zero-gradient condition is applied. At inflow boundaries, the flow vector is specified, while periodic conditions on the sides simulate ganged engines. Current and electric field conditions are established through the electric potential on the boundaries. Details of this procedure have been described in Ref. 10. Briefly, the potential at electrodes is established and specified based on appropriate load factors as described later (the external circuit is not currently solved), whereas at insulators, the normal component of current is set to zero. The sharp variation of ϕ on boundaries at electrode/insulator junctions gives rise to numerical instabilities which propagate into the domain. To suppress these, the boundary values of ϕ are also filtered with the low-pass procedure described in Ref. 11. Numerical implementation in general curvilinear coordinates is not trivial, but high-order numerically stable boundary implementations have been successfully developed in Ref. 10 and are employed in this effort.

IV. General Features and Plasma Environment

The broad features of the flowpath are first explored with reference to Fig. 4, which shows mean and centerline streamwise velocities and Mach number profiles for Case A. Here and later, the term "centerline" is referenced to the computational plane ($\eta = 0.5$, $\zeta = 0.5$), whose trace only approximates the physical centerline of the configuration because of mild asymmetry about the horizontal plane. Various features of the scramjet flowpath are clearly reflected in these profiles. The first two sharp Mach number reductions are attributable to the ramp shock and its reflection off

]

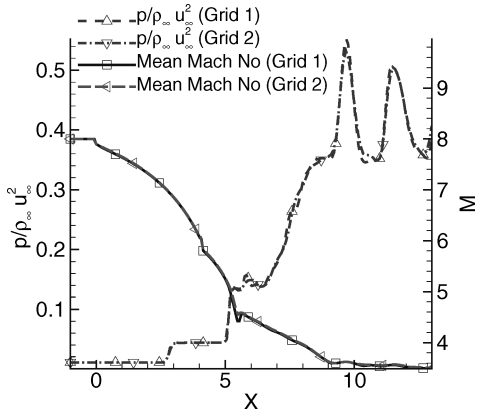

Fig. 5 Effect of grid resolution.

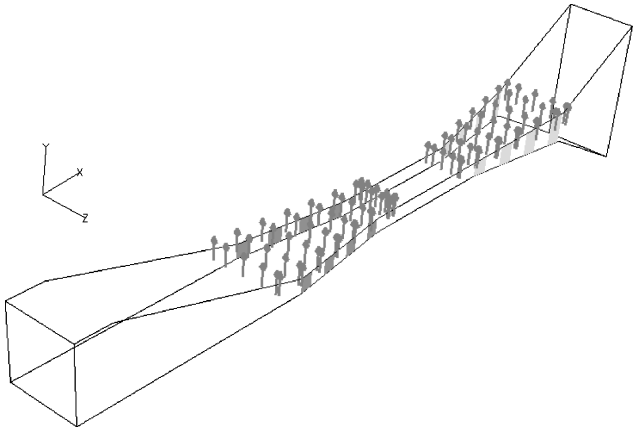

Fig. 6 Imposed magnetic field.

the cowl lip. The horizontal diffuser yields more gradual reductions because of the lower Mach number and the three-dimensionality associated with sidewall shock–boundary layer interactions. The centerline profiles in the isolator region are characterized by undulations associated with a train composed of shocks and expansions in both the horizontal and vertical planes as described later. In most regions, velocity gradients are far smaller than those in the Mach number; note that the mean velocity does not drop below 20% of the freestream value. However, centerline values show much greater variation, with a large decrease at the end of the HD. This is the result of the centerline cutting through a low-energy vortical structure pair arising from complex three-dimensional viscous/inviscid interactions as described below.

A mesh resolution study was performed by also simulating the flow on a coarser $201 \times 41 \times 41$ mesh. Figure 5 exhibits the centerline normalized static pressure and mean Mach number versus streamwise distance. Little perceptible difference is observed between calculations on the two meshes. Peak pressures in the isolator reach about 50 times the freestream pressure but differences observed between the two meshes are restricted to about 3%.

The general features outlined above are employed to choose a suitable plasma environment, which is modeled phenomenologically because a first-principles-based simulation of the full three-dimensional flowpath is not feasible at present. To this end, a uniform magnetic field oriented in the transverse direction and nondimensionalized to unity is assumed as shown in Fig. 6. The field is unperturbed by induced currents because the low-R_σ approximation is invoked. The interaction of currents in the fluid with the external circuit, which is not simulated, occurs through four pairs of segmented electrodes mounted in the HD section to simulate the generator, with a similar arrangement in the nozzle for the accelerator (Fig. 7).

The potential gradients between the electrode surfaces are established from specified load factors and a local reference velocity

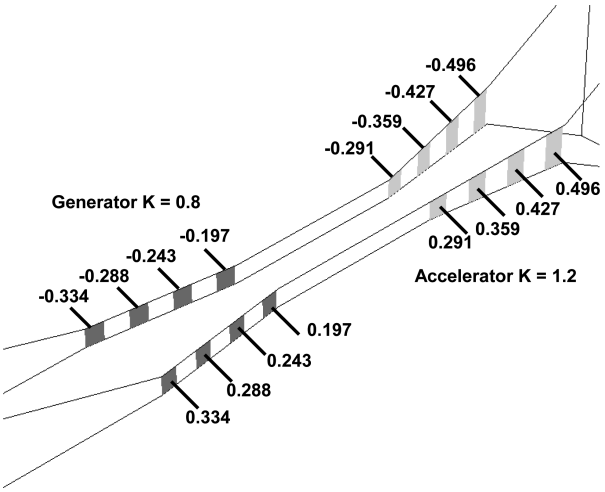

Fig. 7 Electrode potentials in generator and accelerator.

through the relation, $K = (\Delta\phi)/(wU_{\text{local,ref}}B)$, where ϕ is the potential on the electrode, w is the width of the channel at the midpoint of the electrode under consideration, and U_{ref} is determined from the velocity profiles for Case A that were shown in Fig. 4. In the generator, $5.7 < X < 9$, the mean streamwise velocity shows relatively small variations, and a value of U_{ref} of 0.86 is representative. By choosing a load factor of 0.8, the potential on each electrode may be easily determined, as shown in Fig. 7. In the accelerator, $13 < X < 16.3$, although $U_{\text{local,ref}} \sim 0.86$ is a reasonable median value for velocity, its range is much larger and specification of a fixed load parameter is more difficult. However, because the primary purpose is to explore the effect of three-dimensionality rather than to provide engineering specifics, the same reference velocity was chosen and a load factor of 1.2 was chosen for the accelerator. In any event, the actual load parameter at steady state differs modestly from that specified because of velocity changes due to magnetic forces, tending toward unity in both MHD components. The specified electrode potentials, shown in Fig. 7, vary with streamwise distance in a manner proportional to the width of the configuration.

The electrical conductivity, σ, is a strong function of the mechanisms producing ionization. Because ionization through the thermal dissociation path is likely to be small, especially in the generator, some kind of artificial enhancement method is required. Popular candidates, each with its own constraints, are seeding,[2] pulsed electric fields, and e-beam ionization.[23] Models of varying levels of sophistication have been developed for each method but introduce substantial computational load and require further validation before they may be applied to complex three-dimensional problems such as that of interest. At present, therefore, we adopt elements of the phenomenology established in Ref. 1 for e-beams and specify the σ profile as shown in Fig. 8. The distributions are established as products of modified Gaussians (MG) of the form

$$\sigma_1(A, a, s, s_0, n) = Ae^{-a(s-s_0)^n} \tag{8}$$

where A is the peak (set to unity for normalized values), a determines the width as below, s is the distance variable, s_0 is the center, and n is the exponent, which is set to 6. The half-width, a, is determined by specifying a value of conductivity ϵ at a specified distance δ from the center s_0:

$$a = (1/\delta^n)\log(A/\epsilon) \tag{9}$$

The streamwise extent of the conductivity distributions for the generator and accelerator are obtained by specifying MG*s* centered at $x = 7.4$ and $x = 14.7$ (see Fig. 1b) with widths determined from ϵ, δ pairs of $\{10^{-10}, 2.75\}$, respectively. The spanwise and transverse MG*s* are centered in the middle of the channel at each streamwise location $\delta(x) = w(x)/2$, where $w(x)$ is the width of the configuration, and ϵ decides the value of surface conductivity. In the vicinity

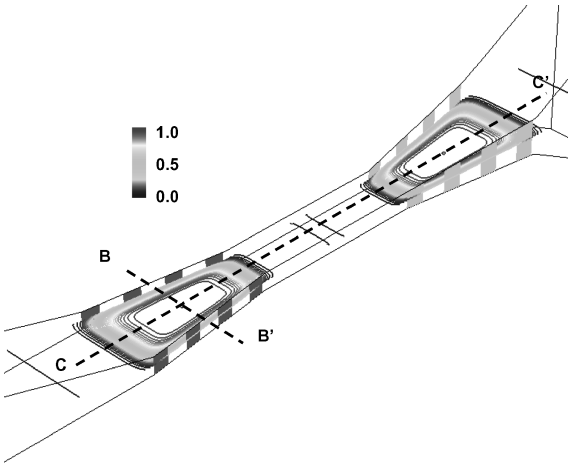

a) Computational *j*-midplane

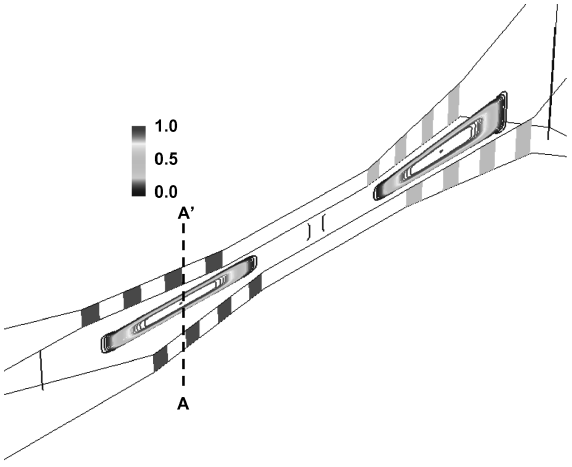

b) Computational *k*-midplane

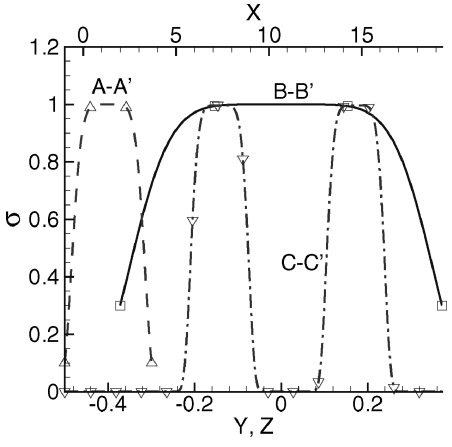

c) Profiles

Fig. 8 Three-dimensional electrical conductivity field established with modified Gaussian products.

of sidewall surfaces, that is, those containing electrodes, the scaled conductivity is 0.3, whereas on the top and bottom walls, the value is 0.1. Profiles of σ through vertical and horizontal cuts are shown in Fig. 8c. Near-electrode effects involving charge separation, such as plasma sheaths, are ignored in the present effort. However, numerical techniques to incorporate such phenomena are presented in Ref. 24.

Heat release due to combustion is modeled through a simple source term in the total energy equation. The spatial distribution is also obtained with MG*s*. The streamwise extent is obtained by choosing a center at $x = 11$ with a half-width of 1.5, as shown

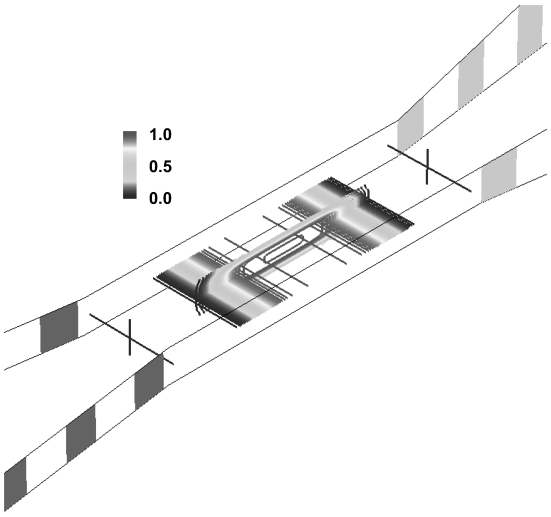

Fig. 9 Heat addition region in combustor.

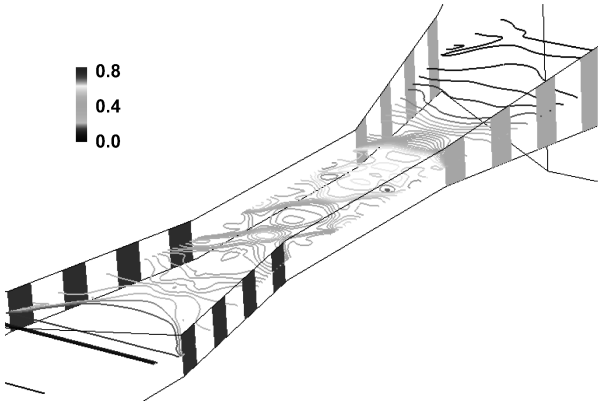

Fig. 10 Pressure contours on j-midplane.

in Fig. 9. In this region, the dimensionless heat release density, $Q_C^* = Q_C L_{\text{ref}}/(\rho_{\text{ref}} U_{\text{ref}}^3)$, is fixed at 20%. This value was chosen to be sufficient to generate discernable trends without causing choking in the channel even with the upstream MHD generator operational.

V. Results

Shock–boundary layer interactions and resultant vortical structures are a major component of the observed flowfield and are analyzed in terms of various three-dimensional kinematic and dynamic features (Section V.A). The complexity of the flow and the mutual interaction with electrical quantities yields different types of nonideal patterns which are elucidated through a study of current, electric, and ponderomotive force fields (Section V.B). The balance of energetic interactions, Section V.C, facilitates analysis of interesting thermodynamic aspects related to the performance of generators and accelerators. Integrated pressure and viscous and magnetic forces are described in Section V.D with emphasis on the change observed with control.

A. Flowfield Structure

The three-dimensional flowfield structure corresponding to Case C is first described with perspective views. Given their importance, primary emphasis is placed on the HD (generator) and nozzle (accelerator) regions. Unless otherwise specified, an artificial ratio 1 : 2 : 2 is applied in perspective views for clarity.

Focusing on Case C, the pressure field on the computational j-midplane is shown in Fig. 10. In this and other figures, the electrodes are marked to provide reference locations. Several discrete anticipated features are readily evident, including the intersection

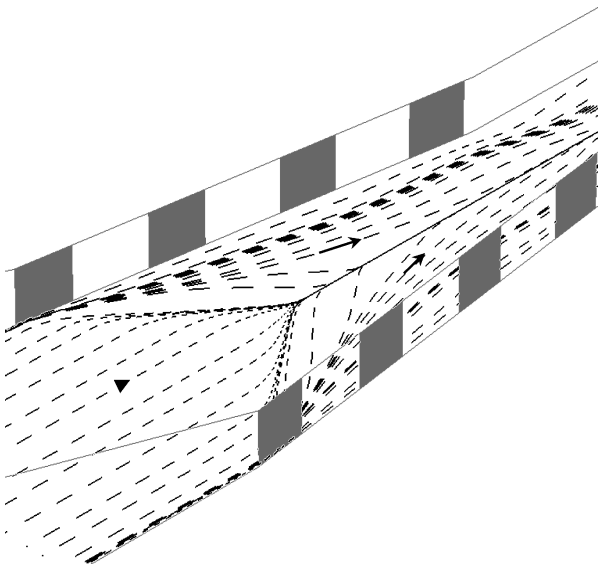

a) Surface oil flow (lower surface)

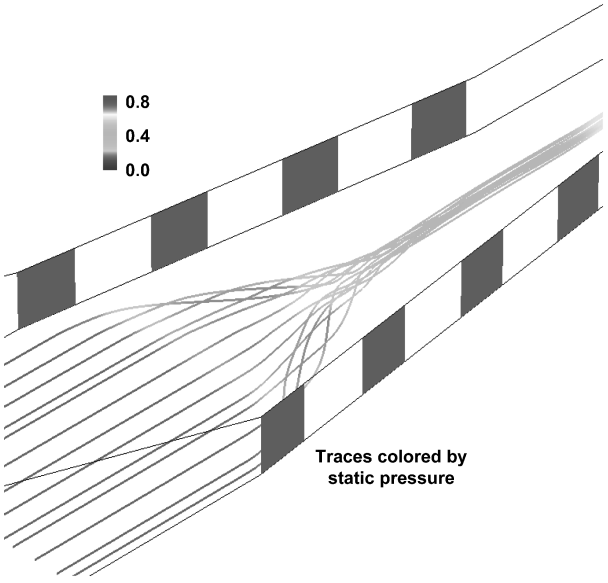

b) Lower vortical flow structure

Fig. 11 Streamline structure in generator region.

of the pitch plane compression shock reflected from the cowl lip. Sharp crossing shocks originating at the entrance to the HD become increasingly diffuse downstream as the flow becomes three-dimensional. The intersection of these shocks with the opposite sidewall boundary layer yields features of shock–boundary layer interactions near the start of the isolator/combustor segment. The numerical procedure captures the subsequent shock and expansion train in a crisp manner. Comparison with Case A (not shown) indicates that the pressure with combustion is substantially higher and the pattern more diffuse in the region prior to the nozzle where the expansion tends to homogenize the flow field. A previous computation employing a similar MHD-assisted inlet but a coarser mesh indicated similar quantitative results and, coupled with the observations of Fig. 4, suggests that the mesh is adequate for the present purpose.

A dominant fluid dynamic feature, with significant impact on MHD operation, originates in the HD as a result of the interaction of the sidewall compresion shock waves with boundary layers on the upper and lower walls. Figure 11a shows the simulated surface oil flow on the lower surface, whereas select streamlines in the corresponding off-surface flow are depicted in Fig. 11b. Lines of coalescence, indicative of separation, are formed near the sidewalls at the HD entrance and sweep spanwise towards the centerline, where

they essentially merge. Lines of divergence, which are not as well defined by their nature, are formed near the corners and indicate flow attachment. Three-dimensional streamlines separating at the line of coalescence lift off the surface and sweep spanwise in a spiraling motion to form a vortical structure, comprised of two counter-rotating cores. The sense of rotation of the left and right structures (looking downstream) is counter clockwise and clockwise, respectively. A similar arrangement of surface oil flow is observed at the upper wall, together with a corresponding off-surface streamline pattern, but is not shown, for brevity. Previous computational and experimental results on relatively stronger swept shock-wave/turbulent boundary layer interactions in the crossing-shock configuration[25] have shown the same primary features. Indeed, turbulent computations on the scramjet flowpath under present consideration, described in Ref. 16, suggest a similar structure. In this context, it may be noted that the presence of a magnetic field damps turbulence, enhancing the qualitative similarity of the laminar and turbulent results in the generator.

The initiation and initial development of the cores of the upper and lower vortical structures are clearly observed in generator Mach number cross-flow contours, shown in Fig. 12a. The low-magnitude regions are observed to be relatively shallow but broad initially and correspond to wall boundary layers. Separation channels this fluid toward the centerline while fluid from above the incoming boundary layer attaches at the line of divergence, entraining high-energy gas near the surface. This effect gradually focuses the vortical structures near the centerline while vertically elongating them. Near the end of the generator, the two cores nearly touch each other.

The evolution of the vortical cores is examined by performing a similar analysis in the isolator/combustor and nozzle regions, as shown in Figs. 12b and 12c. The upper and lower vortical structures essentially merge into a single coherent structure with two horizontally displaced lobes that increase in size as they progress downstream. The boundary layer thickness on the sidewall also increases as the fluid encounters the shock train. Smaller vortical structures are evident at each of the four corners of the duct. These "corner" vortices actually originate in the generator between the line of divergence and the sidewall but show more rapid growth in the combustor and the nozzle. The turbulent simulation described in Ref. 16 yields much thicker boundary layers on the sidewalls and results in choking for the chosen cross-sectional area. Because the accuracy of the turbulence model and the point of transition is uncertain in the complex flowfield under study, those results are not included in this paper. The emphasis is rather on the interaction of the velocity and magnetic fields, which form the primary basis for the ponderomotive force and the energy interaction. The main vortical structure diffuses under the expansion and induced acceleration in the nozzle.

The low-Mach-number vortical regions are also characterized by lower velocities. For completeness and subsequent reference, Fig. 13 shows velocity magnitude contours on selected cross-flow planes (note that a 1:3:3 aspect ratio is applied in this figure) The effect of the viscous/inviscid interaction is clearly significant. Not including the boundary layer regions, highest momentum deficits occur near the centerline, whereas the flow is relatively more uniform elsewhere, resulting in wakelike profiles near the center of the channel.

The primary features described for Case C also exist in Cases A and B. However, quantitative details are substantially different and are characterized by plotting velocity magnitude, Mach number, pressure, temperature, total pressure, and total temperature along the centerline in Fig. 14. Since the centerline traverses through the vortical structure, and is not representative of regions outside of it, another line, corresponding to the streamwise set of gridpoints along computational coordinates $j = 31$, $k = 45$, is also chosen for examination in Fig. 15.

Several important conclusions may be derived from these plots. The effect of three-dimensionality on quantitative details is evident in the wide variation in computed quantities at the two locations: note for example the differences in total temperature along the centerline (which passes through the vortical structure, Fig. 14c) and off centerline (Fig.15c), where the fluid has experienced lesser effects

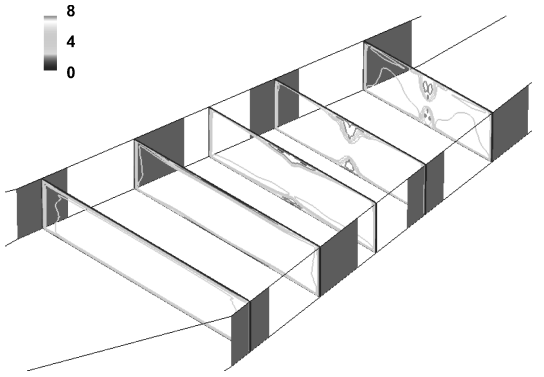

a) Generator

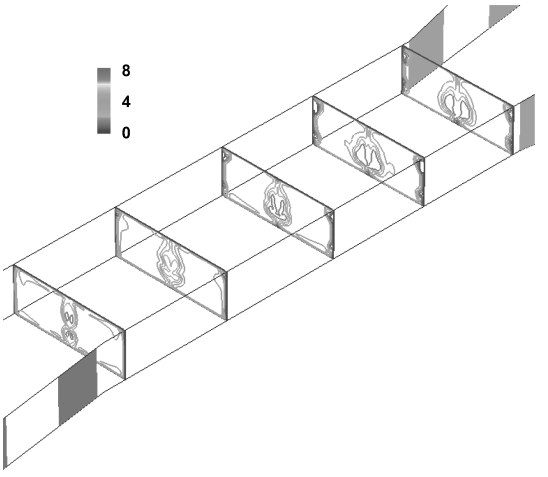

b) Isolator/combustor

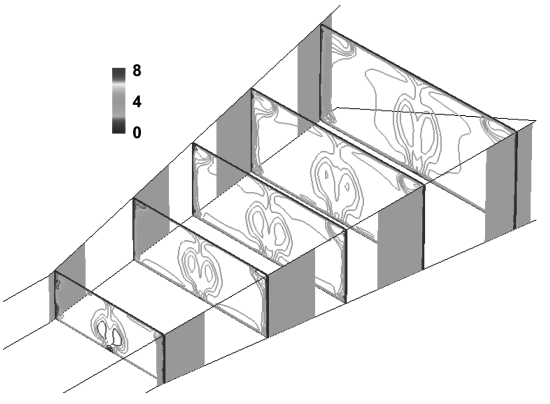

c) Accelerator

Fig. 12 Evolution of vortical structures with Mach number.

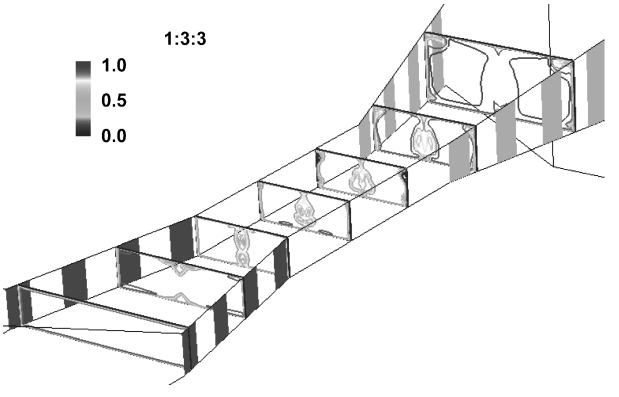

Fig. 13 Velocity magnitude contours at cross-flow stations.

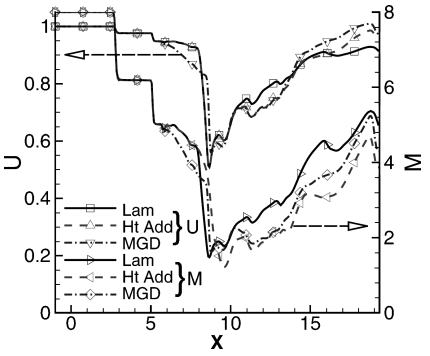

a) Velocity magnitude and Mach number

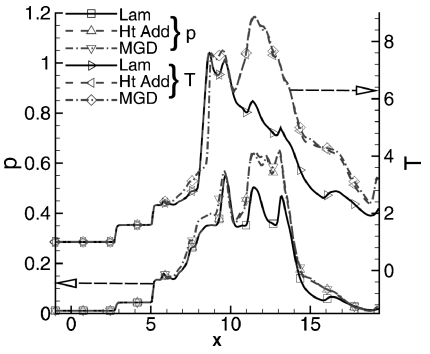

b) Static pressure and temperature

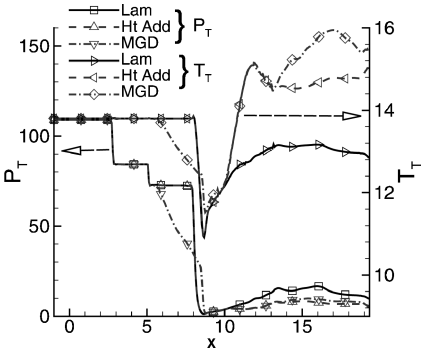

c) Total pressure and temperature

Fig. 14 Variation of fluid dynamic parameters along centerline.

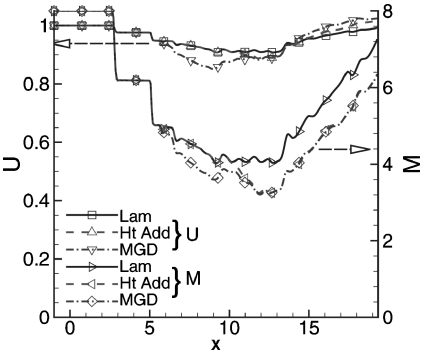

a) Velocity magnitude and Mach number

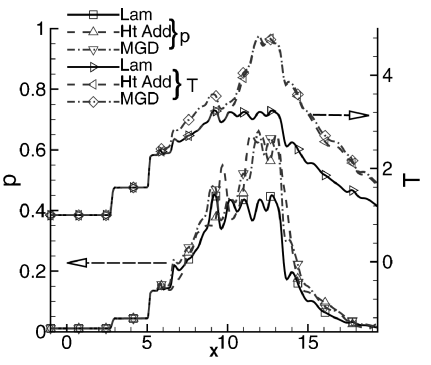

b) Static pressure and temperature

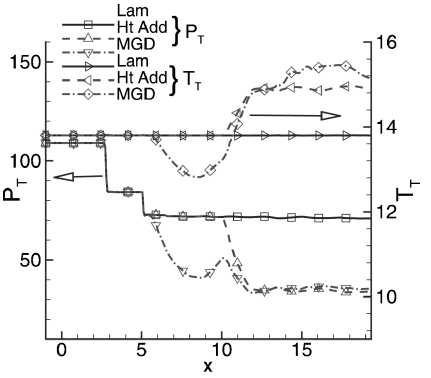

c) Total pressure and temperature

Fig. 15 Variation of fluid dynamic parameters off centerline.

of viscosity. This observation reiterates the unsuitability of lower-dimensional or inviscid calculations for realistic assessments.

The main effects of heat addition may be summarized by comparing Case A ("Baseline") with Case B ("Ht Add"). Focusing on the combustor region, $9 < X < 13$, the Mach number and total pressure are lowered, whereas pressure, temperature and total temperature are increased, particularly outside of the vortical core (Fig. 15). The effect of MHD is more nuanced. Considering the generator first, the velocity magnitude and Mach numbers diminish by about 8% and 0.7, respectively, at the centerline. Equivalent numbers at the off-centerline location plotted are 5% and 0.4. Differences in static pressure and temperature at the downstream end of the generator, $X \sim 9$, remain modest. However, total pressure and temperatures are reduced significantly along both lines plotted. These effects are consistent with work being performed by the fluid—an observation to be further discussed later in the context of energetic interactions. These results indicate that the generator can help reduce inlet length to yield a given reduction in flow velocity and Mach number with lower losses than if accomplished by equivalent shock waves. Further, total temperature reductions in the inlet can modify combustor operation characteristics.

The direct impact of the MHD accelerator is more difficult to characterize because the condition at the entrance to the nozzle is modified by the MHD generator. Nevertheless, some general observations may be made. Very modest MHD-accelerator-induced velocity increments are discernable at both centerline and off-centerline locations, but the Mach number boost is only observed at the former. The total temperature shows substantial increase while the total pressure is very nearly the same. Coupled with further analyses of electromagnetic fields below, the computations show that the accelerator is characterized by significant nonuniformity and nonideal behavior.

B. Current, Electric, and Ponderomotive Force Fields

Select current lines, shaded by magnitude, are shown in Fig. 16a (generator) and Fig. 16b (accelerator) to highlight points of interest. In both regions, current enters and exits the domain primarily through the electrodes, although relatively small magnitudes, less than 5% of peak, are observed even at insulators due to numerical leakage. As was shown in Ref. 10 by considering channel flow with segmented electrodes, the electrode/insulator juncture must be resolved to very high fidelity for numerical stability to be maintained. Such resolution was not affordable in the present work. Consequently, boundary values were filtered to eliminate high-frequency oscillations and the condition $\boldsymbol{n} \cdot \boldsymbol{j} = 0$, required at insulator surfaces, was satisfied only approximately.

Flow separation is not prominent near the first electrode of the generator and the established current follows the anticipated pattern.

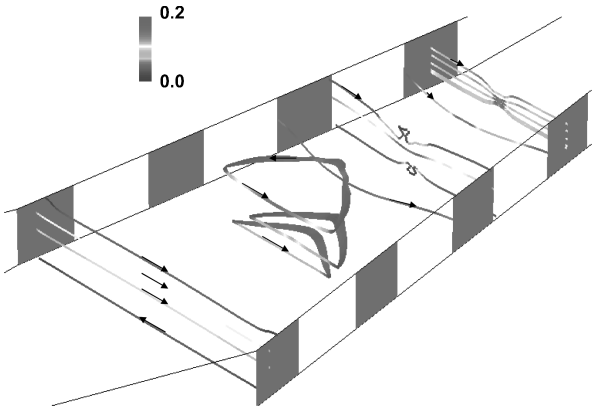

a) Generator

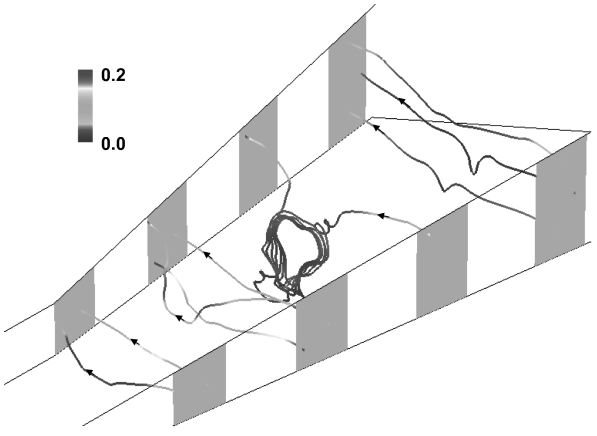

b) Accelerator

Fig. 16 Current paths in generator and accelerator.

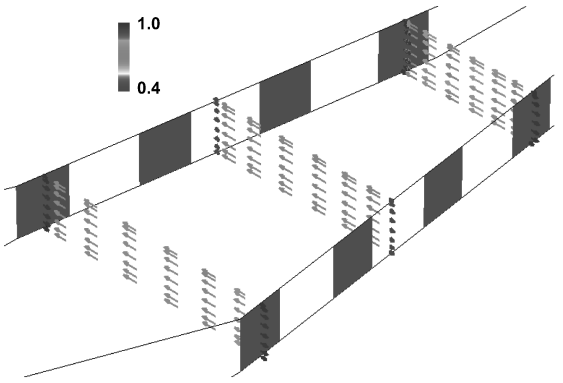

a) Generator

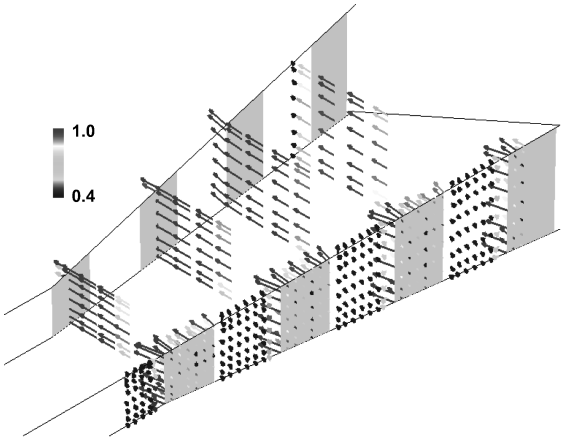

b) Accelerator

Fig. 17 Select electric field vectors.

Because the motional emf, proportional to $\boldsymbol{U} \times \boldsymbol{B}$, is larger by design than the imposed $\boldsymbol{E}$, the current direction is from cathode to anode with values highest near the center and diminishing near the top and bottom walls, where σ is smaller. An interesting feature is current reversal in the layers immediately adjacent to the upper (not shown) and lower walls (note reversed arrow). Here the velocity vanishes because of the no-slip condition and the electric field imposed by the electrodes is dominant. Although no significant impact is observed on the velocity pattern due to this shorting, a possible method of suppressing this phenomenon is to terminate the electrodes away from the upper and lower corners.

The occurrence of three-dimensional separation has a major impact on the current pattern downstream. One effect is the development of eddy current patterns appearing as slightly inclined triangles (Fig. 16a). The streamwise velocity deficit in the vortical structure creates a local region where the motional emf is smaller than the imposed field, thus yielding current reversal at the midspan near the upper and lower walls. Downstream, these eddies are compressed into smaller loops, essentially constricting the dominant current lines in the main (core) flow to the center of the channel, where current magnitude is large. This pinching effect is seen clearly in the current paths emanating from the last electrode.

Three-dimensional effects also have a significant impact on the current pattern in the accelerator (Fig. 16b). Here the current is in the direction of the imposed electric field, as anticipated, but the magnitude diminishes substantially on proceeding toward the nozzle-exit. This effect is mainly attributable to the choice of a load factor based on a constant nominal velocity to compute electrode potentials. In fact, as observed in Fig. 15, the velocity in the nozzle increases by about 10%, thus ensuring that at the downstream end, the accelerator operates at a much lower load factor than specified. The effect of increasing velocity can of course be compensated for by increasing the potential gradient in the downstream direction (thus maintaining the desired constant load factor)—however, this complication was not simulated in the present effort. The existence of recirculating loops of small current intensity is also manifest as are nonuniformities due to the evolution of the vortical cores. In both accelerator as well as generator, current lines originating from the upstream edges of the electrodes show a slight upstream bulge.

Select electric field vectors are shown in Fig. 17. In the generator, Fig. 17a, the field has a simple structure, oriented in the direction imposed by the electrodes. An interesting quirk however is a reversal of the field direction at the electrode itself. The explanation for this is based on the vanishing velocity at the wall due to the no-slip condition. Here $\boldsymbol{U} \times \boldsymbol{B}$ is zero and the observed field reversal is essential to maintain current direction and continuity. The electric field in the region between electrodes is also fairly uniform. Given the current direction, no such reversal is observed in the accelerator, Fig. 17b, where electric field magnitudes are much larger, because they are required to overcome the motional emf. The field is smooth near the first and second electrodes. At the third and fourth electrodes, there is considerable variation, particularly at the upstream edge of the electrode itself.

Since the magnetic field is constant, the ponderomotive force exerted on the gas (Fig. 18) is directly deducible from the current. In most regions of the generator, Fig. 18a, the ponderomotive force opposes the flow and slows it down as desired. The operation is fairly straightforward near the entrance to the generator, where a relatively uniform core exists. The force field is thus relatively uniform near the center of the channel and diminishes near the upper and lower boundaries. Even though the force is not reduced near the electrodes (where the current is maintained through the electrodes), no sidewall separation or other adverse effects are observed, because they are partly offset by the spanwise orientation (toward the electrode) because of the previously mentioned bulging of current lines near the edges of electrodes. The subsequent constriction of current observed in Fig. 16a is accompanied by large body forces near the centerline. Close scrutiny reveals the reversal of force vectors in the center of

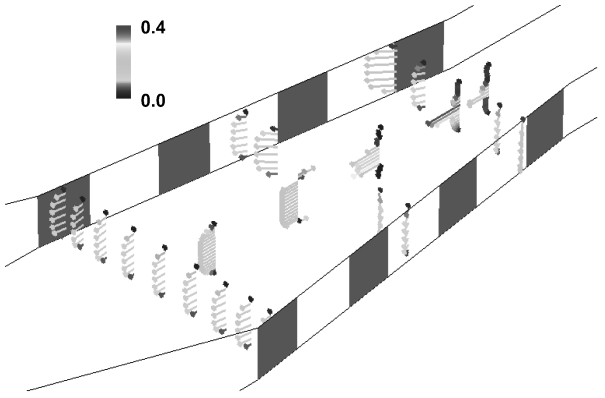

a) Generator

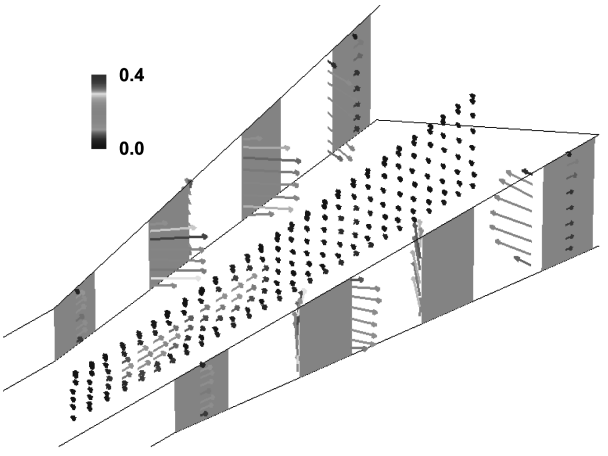

b) Accelerator

Fig. 18 Select ponderomotive force vectors.

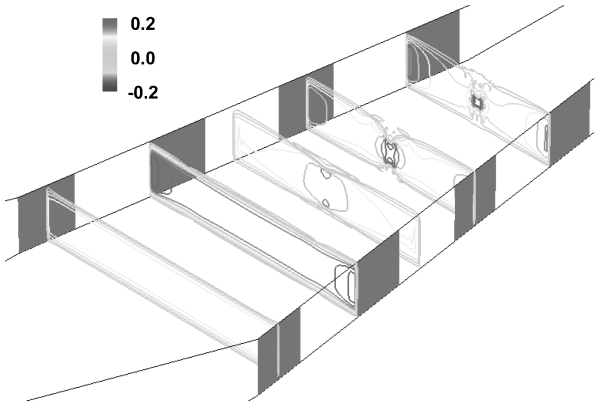

a) Generator

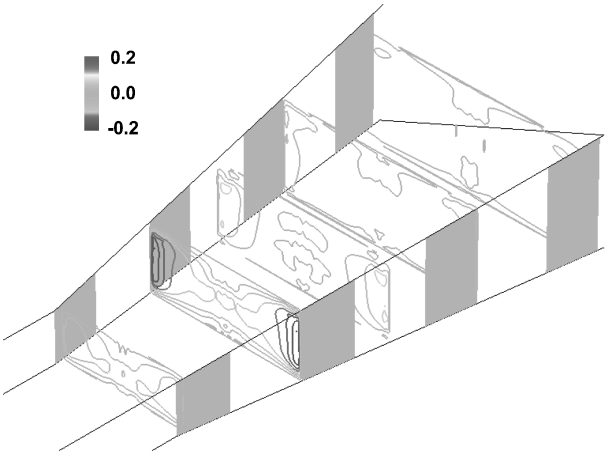

b) Accelerator

Fig. 19 Work term depicted by $j \cdot (U \times B)$ contours.

the channel, very near the upper and lower walls—this is consistent with the current reversals and eddy currents observed earlier—and suggests that MHD generators may suppress separation, after it has occurred, by acting locally as accelerators.

Ponderomotive force vectors in the nozzle, Fig. 18b, accelerate the flow, though their magnitude is generally smaller than that of those in the generator. In the center plane, the force magnitude oscillates in the streamwise direction, being large in electrode cross-flow planes and small where insulators are present. This effect is partly predicated upon a relatively large interelectrode separation being chosen and indicates a need for finer segmentation in the accelerator. Beyond the second electrode, the body forces on the centerline are small—this is also a consequence of the constant load factor assumption noted earlier. Of greater concern, however, are the relatively large values and changes in ponderomotive force vectors that are observed at the edges of each electrode. Analysis of the field suggests that the force changes rapidly from a primarily spanwise and upstream orientation to a streamwise orientation. This is consistent with the earlier noted large local current gradient near the leading edges of the electrodes.

C. Energy Considerations

An important aspect of MHD operation efficiency may be judged from the relative magnitudes of various components of the energy term, $\boldsymbol{E} \cdot \boldsymbol{j}$, which may be decomposed into

$$\boldsymbol{E} \cdot \boldsymbol{j} = \boldsymbol{j} \cdot (\tilde{\tilde{\sigma}}^{-1} \cdot \boldsymbol{j}) - \boldsymbol{j} \cdot (\boldsymbol{U} \times \boldsymbol{B}) \tag{10}$$

The first term on the right represents Joule heating, whereas the second is the work done by ponderomotive forces on the fluid (because $-\boldsymbol{j} \cdot (\boldsymbol{U} \times \boldsymbol{B}) = \boldsymbol{U} \cdot (\boldsymbol{j} \times \boldsymbol{B})$). Distributions of $\boldsymbol{j} \cdot (\boldsymbol{U} \times \boldsymbol{B})$ and the Joule heating term are shown in Figs. 19 and 20, respectively. In the generator, Figs. 19a and 20a, both terms are relatively uniform upstream but gradually develop the same patterns and correlations with other parameters observed earlier. The current constriction near the center of the channel yields higher levels of both Joule heating and work done by the fluid. The ratio of these terms, which determines efficiency, is discussed later with line plots. Although velocity deficits near sidewalls show diminished values of work done by the fluid, Joule heating is higher near electrodes because conductivity is relatively small here but current remains large to accommodate the continuity constraint. With the exception of the near-wall vortical flow region, the values of $\boldsymbol{j} \cdot (\boldsymbol{U} \times \boldsymbol{B})$ are positive, indicating that work is done by the fluid on the external circuit or dissipated into heat.

Energy interactions in the accelerator are shown in Figs. 19b and 20b. Consistent with the noted reduction of effective load factor in the downstream direction, nonnegligible values in the interior are restricted to the region upstream of the second electrode. However, near-electrode heating continues to be significant even up to the end of the third electrode. The work term is negative in most parts of the accelerator, since the current is opposed to the motional emf and both Joule heating and work increase the total energy of the fluid as observed before in Fig. 14. Whereas reversal of operation in the generator was observed in the low velocity structures near the upper and lower walls at midspan, in the accelerator such a reversal with localized deceleration is observed near the electrodes.

A more quantitative assessment of energetic interactions is obtained from line plots of each of the three quantities in Eq. (10). At the centerline, Fig. 21a, significant streamwise variation is evident in all quantities since the design does not facilitate the evolution of a spatially monotonic state. Although the effective load factor must approach unity under the current setup, the effect on the centerline is the opposite (reduced load factor) due to the current constriction observed in Fig. 16a. Generator operation is observed to be

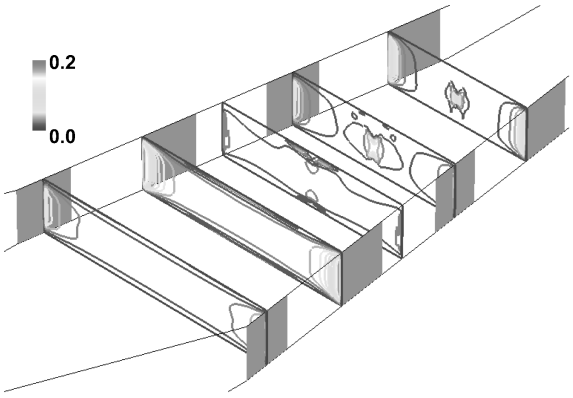

a) Generator

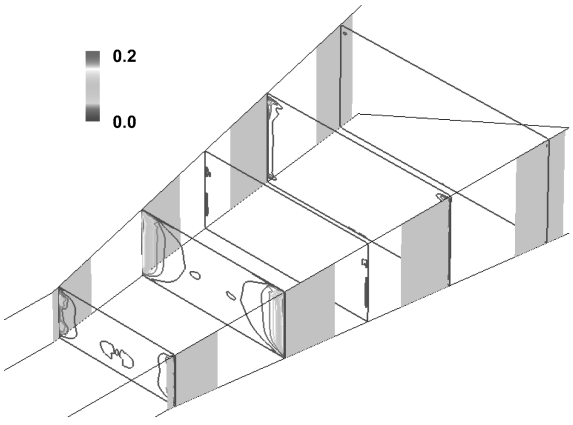

b) Accelerator

Fig. 20 Joule heating contours.

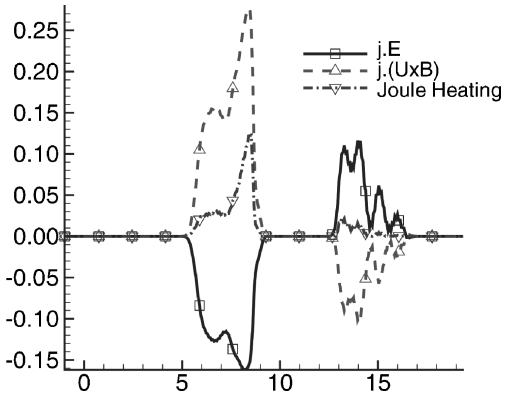

a) Near centerline

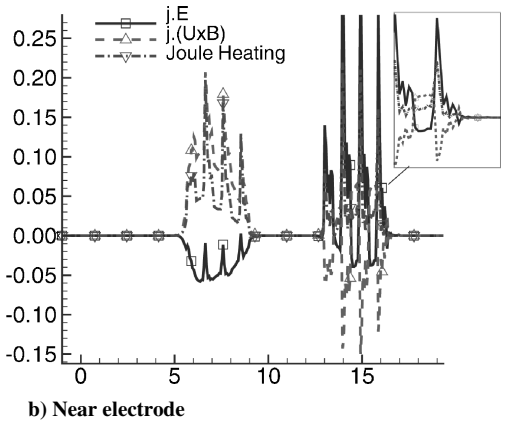

b) Near electrode

Fig. 21 Breakout of energetic terms.

relatively efficient: the largest component is the work done by the fluid, and energy extracted from the flow ($\boldsymbol{j} \cdot \boldsymbol{E}$) is larger in magnitude than the Joule heating term. The energetic interaction is smaller in the accelerator, where the granularity of the electrodes is more evident in the peaks, of which there is one per electrode. The reduction in effective load factor yields much smaller interaction near the third and fourth electrodes. Nonetheless, Joule heating focused locally near the centerline remains a small part of the energy input to the fluid.

The situation is considerably different near the electrodes, however. Figure 21b shows the same quantities at the first point away from the right sidewall. The streamwise undulations are much sharper and more directly correlated with electrode location. Further, Joule heating is relatively large: its magnitude is comparable to that of the work term particularly near leading edges of accelerator electrodes. At several locations the work term exhibits change in sign, which correlates with regions of upstream-oriented body forces observed in Fig. 18.

D. Integrated Parameters

Pressure and viscous forces were integrated over the wetted area to examine the effect of MHD on these components of lift and drag. The pressure force, F_p^*, normalized by $\rho_{\text{ref}} U_{\text{ref}}^2 L_{\text{ref}}^2$, is obtained with

$$\boldsymbol{F}_p^* = \int_{\text{WA}} p^* \hat{n} \, \mathrm{d}A^* \tag{11}$$

where WA is the wetted area, $\hat{n}$ is the normal vector at the surface (directed into the flow), and $\mathrm{d}A$ is the surface area represented by each grid point on the body surface. Viscous forces are obtained with

$$\boldsymbol{F}_v^* = \frac{1}{Re} \int_{\text{WA}} (\bar{\bar{\tau}}^* \cdot \hat{n}) \, \mathrm{d}A^* \tag{12}$$

Figures 22a and b show streamwise and vertical force variation with axial distance for pressure and viscous forces. Positive values correspond to drag in the x direction or lift in the y direction. In the streamwise direction, Fig. 22a, pressure drag accrues from the fuselage ramp and HD regions. MHD operation has only a modest effect on this component. Thrust is obtained primarily from nozzle and thrust surfaces, where the effect of heat addition is prominently observed. Here too, the MHD accelerator has relatively little direct impact on these integrated components. Viscous forces are more consistent along the device length but, except for the isolator/combustor region, are generally smaller than the pressure contributions.

Vertical forces due to pressure are shown in Fig. 22b (viscous forces in this direction are negligible). Pressure forces provide significant lift on the fuselage ramp and in the nozzle while the primary negative lift component arises from the cowl surface up to the start of the HD. Here the pressure on the lower surface is larger because of the reflection of the pitch plane shock off the cowl lip. Oscillatory forces are observed in the HD and isolator section as pitch-plane shocks reflect off the upper and lower channel walls. Spanwise forces are negligible compared to the streamwise and transverse forces and are thus not shown. This is, however, untrue when Hall effects are factored into the analysis.[16,17]

Figure 22c shows variation of the three components of magnetic force, computed through a volume integral:

$$F_B^* = \int_V Q(\boldsymbol{j}^* \times \boldsymbol{B}^*) \, \mathrm{d}V^* \tag{13}$$

Clearly, the dominant force interaction between the flow and the magnet occurs in the streamwise direction. The drag penalty in the generator is highest in the region of the first electrode (where ponderomotive forces are largest) and gradually decreases downstream.

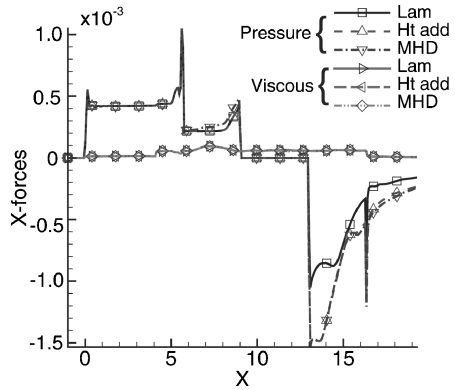

a) *x*-direction

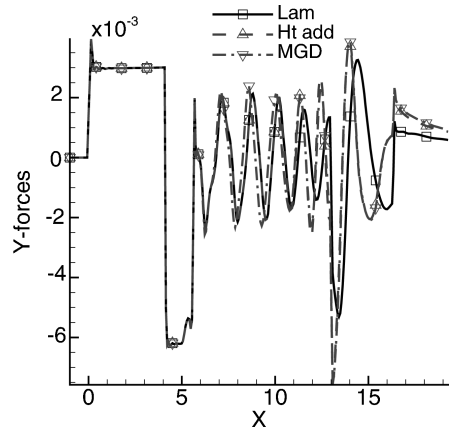

b) *y*-direction

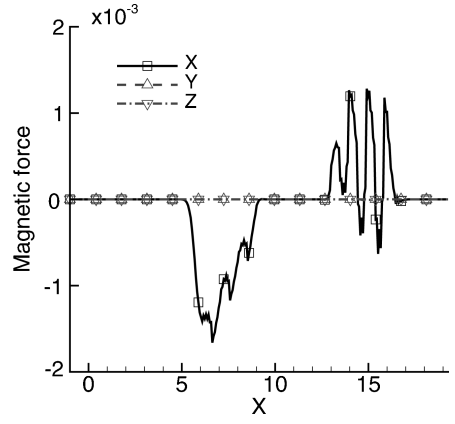

c) Force on magnet

Fig. 22 Integrated forces.

The nonuniformity of the accelerator flow is evident in the rapid oscillations. Although most regions yield thrust, segments near electrode leading edges show a net local drag force because of upstream-oriented body forces observed previously. Overall, peak magnetic force values are comparable to pressure forces.

VI. Conclusions

A representative fully three-dimensional simulated scramjet configuration has been employed to explore various numerical and physical aspects of scramjet operation with and without MHD energy bypass under a specified plasma configuration. For the configuration considered, viscous/inviscid interactions are shown to yield three-dimensional effects that have a significant impact on the established current and ponderomotive force fields. Two-dimensional and inviscid results may therefore yield misleading results. Vortical structures give rise to the formation of near-wall eddy currents and local reversal. Despite these nonuniformities, overall, generator operation is observed to be relatively efficient and suggests that MHD interactions can slow down the fluid in the inlet without large losses, thus reducing its length. Analysis of energy terms suggests that accelerator operation is not as efficient, with significant Joule heating effects in near-wall boundary layers. Integrated parameters reveal several expected trends and show that peak magnetic and pressure forces are comparable to each other and accrue a net drag penalty. The results are qualified by several assumptions, including relatively coarse segmentation, fixed load factors, a specified plasma configuration, frozen flow, and uncertainty in electrical conducting properties of the medium. More precise analysis requires further development and incorporation of more advanced ionization models in a fully self-consistent simulation tool exploiting multiprocessing strategies.

Acknowledgments

The author is grateful for AFOSR sponsorship under tasks monitored by J. Schmisseur and F. Fahroo. The author acknowledges extensive conversations with J. Poggie and J. Shang. Helpful suggestions and comments were also received from several other researchers, including I. Adamovich, D. Davis, M. Hagenmaier, R. MacCormack, S. Macheret, D. Risha, and M. Visbal. This work was also supported in part by a grant of HPC time from the DoD HPC Shared Resource Centers at ASC, CEWES, and NAVO.

References

[1]Macheret, S., Shneider, M., and Miles, R., "Magnetohydrodynamic Control of Hypersonic Flows and Scramjet Inlets Using Electron Beam Ionization," *AIAA Journal*, Vol. 40, No. 1, 2002, pp. 74–81.

[2]Park, C., Bogdanoff, D., and Mehta, U., "Theoretical Performance of a Nonequilibrium MHD-Bypass Scramjet," AIAA Paper 2001-0792, Jan. 2001.

[3]Kuranov, A., Kuchinsky, V., and Sheikin, E., "Scramjet with MHD Control Under "AJAX" Concept. Requirements for MHD Systems," AIAA Paper 2001-2881, June 2001.

[4]Bobashev, S., Mende, N., Sakharov, V., and van Wie, D., "MHD Control of the Separation Phenomenon in a Supersonic Xenon Plasma Flow. I," AIAA Paper 2003-168, Jan. 2003.

[5]Bityurin, V., Bocharov, A., Krasilnikov, A., and Mikhailov, A., "Experimental Study of MHD Electrical Power Generation," AIAA Paper 2003-0377, Jan. 2003.

[6]Gurijanov, E., and Harsha, P., "AJAX: New Directions in Hypersonic Technology," AIAA Paper 96-4609, Nov. 1996.

[7]Kuranov, A., and Sheikin, E., "The Potential of MHD Control for Improving Scramjet Performance," AIAA Paper 99-3535, June 1999.

[8]MacCormack, R., "Flow Calculations with Strong Magnetic Effects," AIAA Paper 2004-0318, Jan. 2004.

[9]Gaitonde, D., and Poggie, J., "Implicit Technique for Three-Dimensional Turbulent Magnetoaerodynamics," *AIAA Journal*, Vol. 41, No. 11, 2003, pp. 2179–2293.

[10]Gaitonde, D., "A High-Order Implicit Procedure for the 3-D Electric Field in Complex Magnetogasdynamic Simulations," *Computers and Fluids*, Vol. 33, No. 3, 2004, pp. 345–374.

[11]Gaitonde, D., "Higher-Order Solution Procedure for Three-Dimensional Nonideal Magnetogasdynamics," *AIAA Journal*, Vol. 39, No. 11, 2001, pp. 2111–2120.

[12]Gaitonde, D., and Poggie, J., "Preliminary Analysis of 3-D Scramjet Flowpath with MGD Control," AIAA Paper 2002-2134, May 2002.

[13]Mitchner, M., and Kruger, C., *Partially Ionized Gases*, Wiley, New York, 1973.

[14]Gaitonde, D., and Poggie, J., "An Implicit Technique for 3-D Turbulent MGD with the Generalized Ohm's Law," AIAA Paper 2001-2736, June 2001.

[15]Macheret, S., Ionikh, Y., Martinelli, L., Barker, P., and Miles, R., "External Control of Plasmas for High-Speed Aerodynamics," AIAA Paper 99-4853, Nov. 1999.

[16]Gaitonde, D., "Three-Dimensional Flow-Through Scramjet Simulation with MGD Energy-Bypass," AIAA Paper 2003-0172, Jan. 2003.

[17]Gaitonde, D., "Effect of Hall-Currents on 3-D Scramjet with MHD Bypass," *Submitted Journal of Propulsion and Power* (submitted for publication).

[18]Roe, P., "Approximate Riemann Solvers, Parameter Vectors and Difference Schemes," *Journal of Computational Physics*, Vol. 43, No. 2, 1981, pp. 357–372.

[19]Holst, T., "Transonic Flow Computations Using Nonlinear Potential Methods," *Progress in Aerospace Sciences*, Vol. 36, No. 1, 2000, pp. 1–61.

[20]Warming, R., and Beam, R., "Upwind Second-Order Difference Schemes and Applications in Aerodynamic Flows," *AIAA Journal*, Vol. 14, No. 9, 1976, pp. 1241–1249.

[21]Schmisseur, J., and Gaitonde, D., "Numerical Investigationof Strong Crossing Shock-Wave/Turbulent Boundary-Layer Interactions," *AIAA Journal*, Vol. 39, No. 9, 2001, pp. 1742–1749.

[22]Gaitonde, D., and Shang, J., "The Structure of a Double-Fin Turbulent Interaction at Mach 4," *AIAA Journal*, Vol. 33, No. 12, 1995, pp. 2250–2258.

[23]Macheret, S., Shneider, M., and Miles, R., "Potential Performance of Supersonic MHD Power Generators," AIAA Paper 2001-0795, Jan. 2001.

[24]Poggie, J., and Gaitonde, D., "Numerical Simulation of Plasma Sheaths in Aerodynamic Applications," AIAA Paper 2002-2166, May 2002.

[25]Gaitonde, D., Shang, J., and Visbal, M., "Structure of a Double-Fin Turbulent Interaction at High Speed," *AIAA Journal*, Vol. 33, No. 2, 1995, pp. 193–200.